CHEMISTRY
A EUROPEAN JOURNAL

DOI: 10.1002/chem.200902037

Quinoidal Oligothiophenes: Towards Biradical Ground-State Species

Rocío Ponce Ortiz,[a, d] Juan Casado,[a] Sandra Rodríguez González,[a] Víctor Hernández,[a] Juan T. López Navarrete,*[a] Pedro M. Viruela,[b] Enrique Ortí,*[b] Kazuo Takimiya,[c] and Tetsuo Otsubo[c]

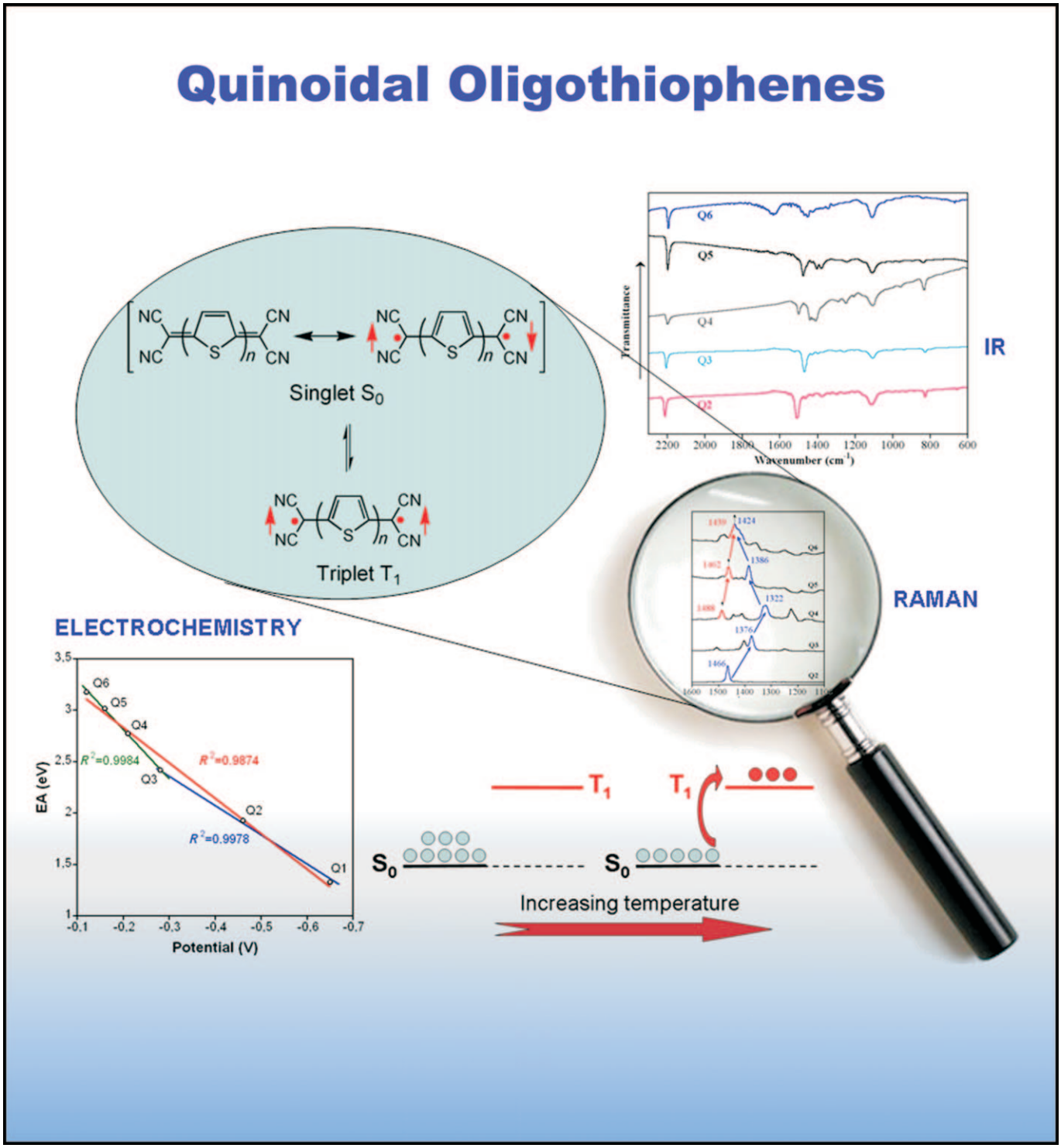

Abstract: A family of quinoidal oligothiophenes, from the dimer to the hexamer, with fused bis(butoxymethyl)cyclopentane groups has been extensively investigated by means of electronic and vibrational spectroscopy, electrochemical measurements, and density functional calculations. The latter predict that the electronic ground state always corresponds to a singlet state and that, for the longest oligomers, this state has biradical character that increases with increasing oligomer length. The shortest oligomers display closed-shell quinoidal structures. Calculations also predict the existence of very low energy excited triplet states that can be populated at room temperature. Aromatization of the conjugated carbon backbone is the driving force that determines the increasing biradical character of the ground state and the appearance of low-lying triplet states. UV/Vis, Raman, IR, and electrochemical experiments support the aromatic biradical structures predicted for the ground state of the longest oligomers and reveal that population of the low-lying triplet state accounts for the magnetic activity displayed by these compounds.

Keywords: biradicals · density functional calculations · electronic structure · oligothiophenes · vibrational spectroscopy

Introduction

In the last few years, quinoidal oligothiophenes have received great attention in the field of organic electronics due to their good behavior as semiconductors in organic field-effect transistors (OFETs).[1] Their small band gaps and amphoteric redox behavior[2] lead to stabilization of both electron (n-type semiconductor) and hole carriers (p-type semiconductor), which meets the key requirement of ambipolar response for complementary circuits. Furthermore, their remarkable processability, conferred by easy β-functionalization, allows their layer deposition by inexpensive solution-based techniques such as spin coating and roll-to-roll printing.[3]

Recently, Takahashi et al. synthesized a new family of quinoidal oligothiophenes (Q*n*) with chain lengths ranging from two to six thiophene rings in which each thiophene unit is fused with a bis(butoxymethyl)cyclopentane group (see Scheme 1).[4] The substituted fused ring is especially helpful for solubilization,[5] facilitating the synthesis of these extended thienoquinoid compounds and improving their processability. Previously reported thienoquinoid oligomers end-capped with dicyanomethylene groups were no longer than tetramers.[6,7] The longest members of the Q*n* series, Q5 and Q6, display ESR activity in solution and were proposed to be in equilibrium with a magnetically active biradical species.[4] Low magnetic activity has also been reported for shorter oligomers in the solid state.[8] In a recent work, Raman spectroscopy and quantum chemical calculations have evidenced the biradicaloid character of long quinoidal oligothiophenes.[9] The fact that these oligomers are magnetically active opens the possibility of envisaging long quinoidal oligothiophenes as candidates for organic spintronics,[10] where a combination of electron/hole transport and magnetic response is required.

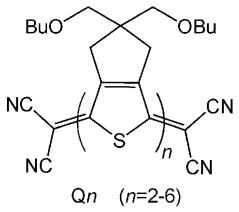

Q*n* (*n*=2-6)

Scheme 1. Chemical structure of the family of thienoquinoid compounds Q2–Q6.

Herein, to carefully define the nature of the ground state of quinoidal systems, we investigate the electronic and molecular structures of quinoidal oligothiophenes Q2 to Q6. In general, the electronic ground state of compounds with

[a] Dr. R. Ponce Ortiz, Dr. J. Casado, S. Rodríguez González, Prof. V. Hernández, Prof. J. T. López Navarrete
Departamento de Química Física
Universidad de Málaga
Campus de Teatinos s/n
Málaga 29071 (Spain)
Fax: (+34) 952132000
E-mail: teodomiro@uma.es

[b] Prof. P. M. Viruela, Prof. E. Ortí
Instituto de Ciencia Molecular
Universidad de Valencia
Valencia 46071 (Spain)
Fax: (+34) 963543274
E-mail: enrique.orti@uv.es

[c] Dr. K. Takimiya, Prof. T. Otsubo
Department of Applied Chemistry, Hiroshima University
Higashi-Hiroshima 739-8527 (Japan)

[d] Dr. R. Ponce Ortiz
Current address: Department of Chemistry
Northwestern University
2145 Sheridan Road, Evanston, IL, 60208 (USA)

Supporting information for this article is available on the WWW under http://dx.doi.org/10.1002/chem.200902037. It contains total energies calculated for Q*n* compounds as closed-shell singlets, open-shell singlets, triplets, and closed-shell dianions (Table S1), optimized bond lengths for Q2–Q4 in the S_0 and T_1 states (Figures S1 and S2), optimized bond lengths for neutral, dianionic, and dicationic species of Q4 and Q6 (Figure S3), RB3LYP/6-31G** simulations of the IR spectra of Q2–Q6 (Figure S4), UB3LYP(BS)/6-31G** simulations of the Raman spectra of Q4–Q6 (Figure S5).

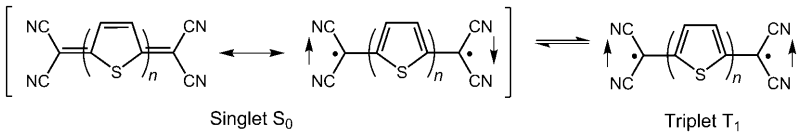

Scheme 2. Kekulé and biradical resonance structures proposed for the singlet ground state of long quinoidal oligothiophenes in equilibrium with the triplet species.

large HOMO–LUMO gaps is well-described by a single closed-shell electron configuration. In contrast, in large quinoidal systems with small HOMO–LUMO gaps, it is essential to consider that electrons can be easily promoted from the HOMO to the LUMO and, as a consequence, the ground state may have biradical character.[11] Under this assumption, the singlet ground state S_0 of the systems under study must be represented by resonance of the closed-shell quinoid Kekulé structure and the pseudo-aromatic biradical form displayed in Scheme 2. The relative weight of these two forms would determine the biradical contribution to the electronic ground state. Furthermore, to explain the appearance of magnetic signals in the EPR experiments on the longest systems,[4] we consider a thermal equilibrium between S_0 and a low-lying triplet state (T_1) energetically populated at room temperature through rapid $S_0 \rightarrow T_1$ intersystem crossing (see Scheme 2).

The aim of this work is twofold. First, the nature of the electronic ground state is determined by using electronic and vibrational spectroscopy, electrochemistry, and quantum chemical calculations. Second, the population of the lowest-energy triplet state is investigated by using thermally dependent Raman spectroscopy with the aid of theoretical calculations. The main goal is to understand the molecular and electronic structures of these novel quinoidal systems and improve knowledge of their magnetic nature. The in-depth understanding of their structural and electronic properties is a requirement for the design of new improved organic molecules suitable for spintronics.

Results and Discussion

Optimized geometries and relative energies of the singlet and triplet states: Table 1 reports the energy differences between the spin-unrestricted (open-shell, OS) and spin-restricted (closed-shell, CS) solutions of the singlet ground state S_0 of Q*n* compounds estimated by DFT B3LYP/6-31G** calculations in the gas phase and in chloroform solution. Energy differences between the singlet (most stable in solution) and the first triplet state T_1 are also included.

Table 1. Relative energies [kcal mol^{-1}] for the S_0 and T_1 states of compounds Q2–Q6 (B3LYP/6-31G**).

	ΔE(OS−CS)[a]			ΔE(T_1−S_0)[b]	
	gas phase	$CHCl_3$	$\langle S^2 \rangle$[c]	gas phase	$CHCl_3$
Q2	0.00		0.00	16.97	17.95
Q3	0.00		0.00	9.88	11.15
Q4	−0.41	−0.13	0.51	5.07	6.17
Q5	−2.03	−0.55	0.86	2.60	3.31
Q6	−4.10	−1.87	1.00	1.35	2.61

[a] Open-shell (OS) UB3LYP(BS) singlet energy minus closed-shell (CS) RB3LYP singlet energy. [b] UB3LYP triplet energy minus singlet energy (OS singlet for Q4, Q5 and Q6). [c] Spin contamination ($\langle S^2 \rangle$ values before annihilation) is given for the OS solution of S_0.

Theoretical results indicate that, in the gas phase, the ground-state electronic structure of the shortest oligomers Q2 and Q3 is well described by the closed-shell solution, since almost no difference is found between the OS and CS solutions. On increasing the chain length, the fact that the OS solution becomes more stable than the CS one (−0.41 kcal mol^{-1} for Q4, −2.03 kcal mol^{-1} for Q5, and −4.10 kcal mol^{-1} for Q6) indicates increasing biradical character of the singlet ground state for long quinoidal systems. The same trend is found in chloroform solution (PCM model), although the energy differences between the two theoretical solutions are smaller in the presence of the solvent.

A second consequence derived from the narrowing of the HOMO–LUMO gap (Q2: 2.16, Q3: 1.67, Q4: 1.33, Q5: 1.06, Q6: 0.83 eV for S_0 at the RB3LYP level) as the length of the oligomer increases is stabilization of the lowest-lying triplet state which is in thermal equilibrium with the singlet ground state. In the gas phase, the energy difference between T_1 and S_0 is estimated to be only 2.60 and 1.35 kcal mol^{-1} for Q5 and Q6, respectively. Slightly higher values (3.31 and 2.61 kcal mol^{-1}) are obtained in chloroform.

Figure 1 shows the optimized bond lengths calculated for the S_0 (RB3LYP and UB3LYP(BS) solutions) and T_1 (UB3LYP) states of Q5 and Q6. The degree of quinoidization/aromatization of the conjugated backbone can be easily quantified from the C–C single/double bond length alternation (BLA).[12] The BLA parameter is calculated for each thiophene ring as the difference between the length of the C_β–$C_{\beta'}$ bond and the average of the C_α–C_β and $C_{\alpha'}$–$C_{\beta'}$ bonds. A quinoidal ring is thus characterized by a negative BLA value, while an aromatic ring shows a positive BLA value. The BLA parameter thus illustrates how the quinoid/aromatic character of the molecule varies with the length of the oligomer and with the electronic state (Table 2).

Table 2 shows that the BLA parameter drastically changes on increasing the size of the oligomer and depends on the nature of the electronic state. RB3LYP optimizations of S_0 yield well-defined quinoidal geometries for Q2 to Q6 with short C_α–$C_{\alpha'}$ and C_β–$C_{\beta'}$ bonds and long C_α–C_β bonds (see Figure 1 and Figures S1 and S2 in the Supporting Information). Open-shell optimizations of S_0 converge to the RB3LYP geometries for Q2 and Q3 and lead to less quinoidal structures for Q4 to Q6, which are better described by the OS solutions. The effect is more pronounced as the oligomer lengthens owing to the larger weight of the biradical form displayed in Scheme 2 in describing S_0. Aromatization of the conjugated backbone decreases on going from the

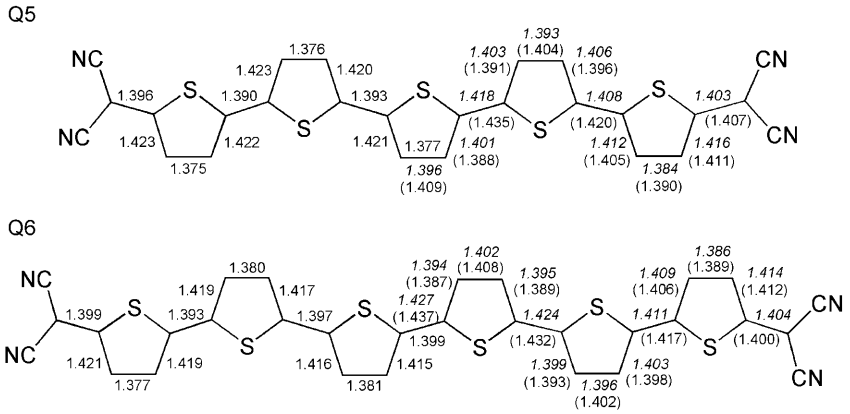

Figure 1. B3LYP/6-31G** optimized bond lengths [Å] for Q5 (C_{2v}) and Q6 (C_{2h}). Values on the left side of the molecule refer to the closed-shell RB3LYP geometry of the singlet ground state S_0. Values in the right side of the molecule refer to the open-shell UB3LYP(BS) geometry of the singlet ground state S_0 (in italics) and to the open-shell UB3LYP geometry of the triplet state T_1 (in parentheses). The bis(butoxymethyl)cyclopentane rings preserve the same geometry for both states and have been omitted for simplicity.

Table 2. BLA values [Å] estimated from the optimized geometries of S_0 (CS and OS solutions) and T_1 for compounds Q2 to Q6. For S_0, the values corresponding to the most stable solution are listed in bold.

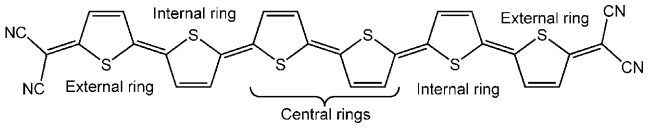

Compound		S_0 (CS)	S_0 (OS)	T_1
Q2		**−0.070**	−0.070	+0.011
Q3	central ring	**−0.062**	−0.062	+0.020
	external ring	**−0.060**	−0.060	−0.005
Q4	internal ring	−0.053	**−0.032**	+0.021
	external ring	−0.053	**−0.041**	−0.014
Q5	central ring	−0.044	**−0.005**	+0.021
	internal ring	−0.046	**−0.012**	+0.011
	external ring	−0.048	**−0.030**	−0.018
Q6	central ring	−0.035	**+0.008**	+0.020
	internal ring	−0.038	**−0.005**	+0.006
	external ring	−0.043	**−0.026**	−0.020

inner to the outer thiophene rings and contributes to stabilization of a biradical singlet as the ground state in these systems.

In the T_1 state, the geometries of compounds Q2 to Q6 all show further aromatization that is also confined to the middle of the oligomer. For Q6, the geometry of the T_1 state strongly resembles the OS geometry of the S_0 state (maximum differences of 0.010 Å, see Figure 1) owing to the pronounced biradical character of the S_0 state for this oligomer. The aromatization process enlarges to a greater extent the inter-ring bonds of the central part of the molecule, and the planarity of the backbone can be lost in these open-shell structures.

Figure 2 shows the atomic spin densities calculated for the S_0 (OS solution) and T_1 states of Q6 as a representative example. The spin-density distributions are similar for both states and indicate that the two unpaired electrons mainly reside in the outer parts of the oligomer with antiparallel spins for S_0 and parallel spins for T_1. For S_0, the terminal dicyanomethylene groups accumulate net spin densities of ±0.38, and the spin density of the thiophene groups decreases on going from the outer (± 0.28), to the intermediate (± 0.14), and to the central or innermost rings (±0.04). For T_1, the unpaired spins are fully localized on the main backbone, and positive spin densities of 0.42, 0.32, 0.16, and 0.10 are calculated for the $C(CN)_2$ groups and the three types of thiophene rings, respectively. The maximum spin density is

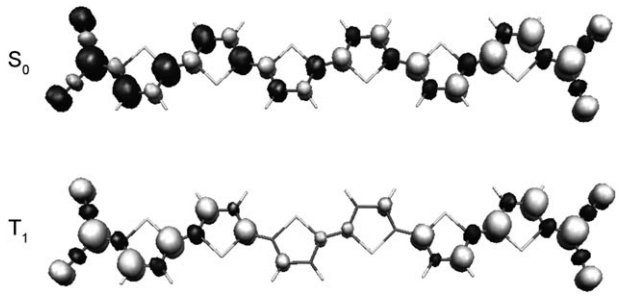

Figure 2. Spin densities calculated at the UB3LYP/6-31G** level for open-shell S_0 and T_1 states of Q6. White and black surfaces represent positive and negative spin densities, respectively. Bis(butoxymethyl)cyclopentane moieties are omitted because they make only small contributions.

over the central carbon atom of the $C(CN)_2$ groups both for S_0 (0.28) and T_1 (0.31). These data are in agreement with aromatization of the central part of the Q6 skeleton for both S_0 and T_1 biradical states and support the chemical structures depicted in Scheme 2 for both states.

Optical spectra and TDDFT calculations: Figure 3 shows the electronic absorption spectra recorded for Q2–Q6 in THF solution.[4] The longest-wavelength absorption band corresponds to a very intense feature that redshifts and increases in intensity on augmenting the length of the oligomer, except for Q6, for which the molar extinction coefficient is lower than for Q5. Table 3 lists the vertical excitation energies and oscillator strengths f calculated for the most intense electronic transitions by using the TDDFT approach. Closed-shell RB3LYP calculations correctly predict the existence of a low-energy intense band associated with the HOMO→LUMO excitation that increases in intensity with increasing oligomer size. The energies calculated for this excitation redshift from 2.45 eV (f=1.24) for Q2 to 1.24 eV (f=3.34) for Q6 and are in good agreement with the experimental values obtained from λ_{max} (see Table 3).

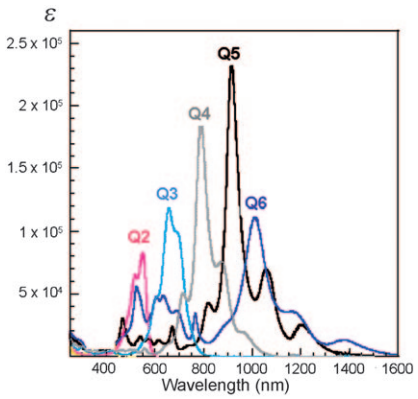

Figure 3. Electronic absorption spectra of quinoidal systems Q2–Q6 recorded in THF solution.

No other electronic transition with significant intensity ($f>0.1$) is calculated below 3.10 eV (above 400 nm).

The intense absorption observed experimentally is therefore assigned to the HOMO→LUMO excitation. The HOMO and the LUMO are of π nature, as expected, and spread over the whole π-conjugated backbone. As illustrated in Figure 4 for Q4, the topologies of these orbitals are reversed with respect to those observed for aromatic oligothiophenes due to the quinoid structure of the backbone. This reversal is accompanied by drastic narrowing of the HOMO–LUMO gap, which explains the redshift of the absorption band of quinoidal systems with respect to their homologues with aromatic structures. The absorption maxima of Q5 and Q6 actually appear in the NIR region at 913 and 1012 nm, respectively.

The topologies of the frontier molecular orbitals also reveal that π–π* HOMO→LUMO excitation does not imply any significant intramolecular charge transfer, since the two dicyanomethylene groups equally participate in both frontier orbitals. The absence of intramolecular charge transfer is experimentally supported by the presence of vibronic components for the aforementioned band (see Figure 3). Vibronic structure is usually observed for the π–π* $S_0 \rightarrow S_1$ band in aromatic oligothiophenes,[13] but does not appear in oligothiophenic systems where the corresponding excitations involve charge transfer.[14]

The TDDFT RB3LYP calculations considering a CS description of S_0 predict that the oscillator strength of the $S_0 \rightarrow S_1$ transition regularly increases with increasing oligomer length (see Table 3) and does not reproduce the decrease in intensity experimentally observed on passing from Q5 to Q6. Furthermore, CS calculations do not account for the group of less intense bands that Q5 and Q6 exhibit in the visible region (450–750 nm, see Figure 3). This disagreement suggests that the CS solution is not sufficient to explain the electronic spectra of the longest quinoidal oligothiophenes.

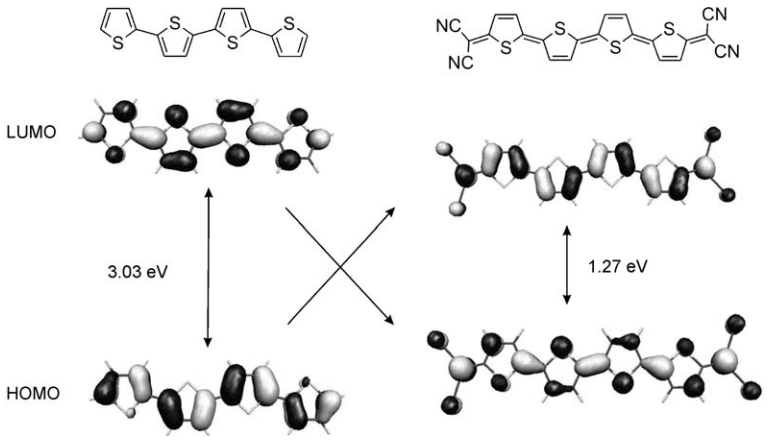

Figure 4. Electron-density contours [0.03 e bohr^{-3}] calculated for the frontier molecular orbitals of aromatic quaterthiophene (T4) and quinoidal quaterthiophene (Q4) at the RB3LYP/6-31G** level. The bis(butoxymethyl)cyclopentane rings in Q4 make no contribution and have been omitted for simplicity.

Table 3. Observed and calculated transition energies (λ [nm] ΔE [eV]) and oscillator strengths f for the most intense electronic absorption bands.

	Exptl[a]		Singlet–Singlet (CS)[b]			Singlet–Singlet (OS)[c]			Triplet–Triplet[d]		
	λ_{max}	ΔE	λ	ΔE	f	λ	ΔE	F	λ	ΔE	f
Q2	548	2.26	507	2.45	1.24						
Q3	657	1.89	621	2.00	1.79						
Q4	788	1.57	739	1.68	2.35	818	1.52	0.88	942	1.32	0.21
			326	3.80	0.14	745	1.66	0.79	605	2.05	1.68
						576	2.15	0.59			
Q5	913	1.36	863	1.44	2.89	942	1.32	1.46	1025	1.21	0.29
			368	3.37	0.13	607	2.04	1.17	665	1.86	1.94
									471	2.63	0.27
Q6	1012	1.22	1001	1.24	3.34	1057	1.17	1.39	1095	1.13	0.39
			503	2.47	0.18	641	1.93	1.56	720	1.72	2.03
			405	3.06	0.19	543	2.28	0.16	527	2.35	0.56

[a] Experimental data from ref. [4], measured in THF. [b] Time-dependent RB3LYP/6-31G** calculations. [c] Time-dependent UB3LYP(BS)/6-31G** calculations. [d] Time-dependent UB3LYP/6-31G** calculations.

To account for these discrepancies, the excited states of Q4, Q5, and Q6 were recalculated at the UB3LYP(BS)/6-31G** level, which takes into account the biradical character of S_0 (Table 3). UB3LYP(BS) calculations predict an intense electronic transition in the near-infrared for Q4 (818 nm, $f=0.88$), Q5 (942 nm, $f=1.46$), and Q6 (1057 nm, $f=1.39$), in very good agreement with experimental λ_{max} values, and reproduce the intensity lowering observed from Q5 to Q6. In addition, they reveal the appearance of new electronic absorptions in the 500–800 nm range, as recorded in the experimental spectra (Figure 3). These results support the biradical character of S_0 predicted for the longest oligomers and especially for Q5 and Q6.

For these oligomers, the energy difference between S_0 and T_1 is very small ($<2.60\,kcal\,mol^{-1}$) and the T_1 state should be partially populated at room temperature. Therefore, triplet–triplet absorptions from T_1 would also contribute to the electronic spectra. Time-dependent UB3LYP calculations of the $T_1 \rightarrow T_n$ transitions predict intense $T_1 \rightarrow T_4$ transitions for Q5 (665 nm, $f=1.94$) and Q6 (720 nm, $f=2.03$) in the visible, and less intense transitions in the near-infrared (Q5: 1025 nm, $f=0.29$; Q6: 1095 nm, $f=0.56$) and around 500 nm (see Table 3). These results suggest that the spectra depicted in Figure 3 for Q5 and Q6 also comprise the optical absorptions of the molecules populating the T_1 state, in thermal equilibrium with S_0, which contribute both to the bands in the visible and to those in the near-infrared.

Photophysical properties: Figure 5 displays the absorption and emission spectra of Q2 and Q3 recorded in 2-methyltetrahydrofuran at low temperatures starting from 25 °C. Fluorescence spectra could not be obtained for the longest oligomers because of the 900 nm upper wavelength detection limit of the fluorimeter; Q4, Q5, and Q6 absorb in the region around 900 nm and fluorescence should appear, if takes place, at lower energies.

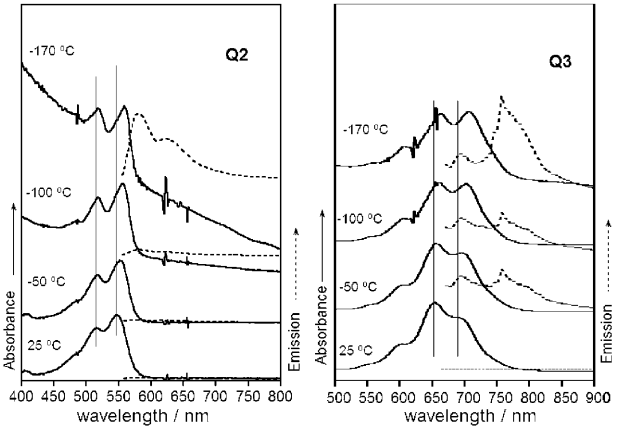

Figure 5. Low-temperature absorption and emission spectra of Q2 and Q3 in 2-methyltetrahydrofuran. Absorption spectra are normalized to that at room temperature. Fluorescence spectra are shown as-recorded.

On cooling, a 12 nm redshift is measured for the absorption band at 547 nm of Q2, while the component at 516 nm remains almost unaltered. More important modifications are detected in the absorption spectrum of Q3, since the lowest-energy peak of the three-component band at 687 nm redshifts by 20 nm on cooling and becomes the strongest one at −170 °C. The absorption registered at 655 nm at room temperature also redshifts to 663 nm at −170 °C. Interestingly, much smaller changes are observed in the emission spectra (1–3 nm shift on cooling). The notable facts are that fluorescent emission appears only at low temperatures and that Q2 is more fluorescent than Q3. Though fluorescent quantum yields were not measured at low temperatures, the absolute intensity and the resolution of the fluorescence spectrum of Q2 are larger than those observed for Q3.

As discussed above, Q2 and Q3 have a quinoid structure in the S_0 state. The double-bond character of the inter-ring bonds restricts internal rotation around the C_α–$C_{\alpha'}$ bonds and the oligomers are essentially planar. Q2 and Q3 become more aromatic and therefore more flexible on passing to the first singlet excited state S_1. This state results from the HOMO→LUMO excitation (see Figure 4), which has a completely different effect on the molecular geometry depending on the nature (aromatic or quinoid) of the system. Figure 6 compares the optimized geometries of S_0 and S_1 calculated for Q3 and α-terthiophene (T3). For Q3, the population of the LUMO determines the aromatization of the molecular structure, and the inter-ring bonds lengthen from 1.381 Å in S_0 to 1.419 Å in S_1. For T3, excitation to S_1 implies quinoidization of the molecule, and the C_α–$C_{\alpha'}$ bonds shorten from 1.447 Å in S_0 to 1.393 Å in S_1. Q2 and Q3 are predicted to be planar in the S_1 state. However, the lengthening of the C_α–$C_{\alpha'}$ bonds allows for twisted conformations at a low energy cost (for instance, a twist of 30° around the central C_α–$C_{\alpha'}$ bond of Q2 has an energy cost of only $0.94\,kcal\,mol^{-1}$), and some conformational disorder can be expected at room temperature in the S_1 state.

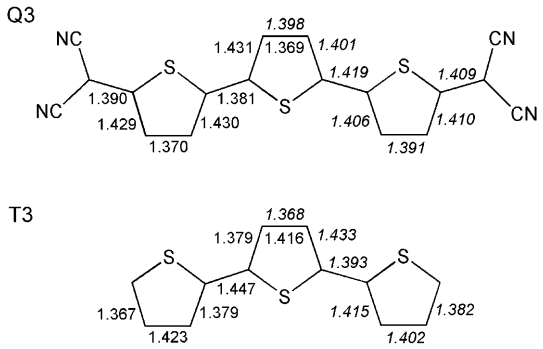

Figure 6. B3LYP/6-31G** optimized bond lengths [Å] for Q3 and T3 in the S_0 (left side of the molecule) and S_1 (right side of the molecule, in italics) states (C_{2v} symmetry). The bis(butoxymethyl)cyclopentane rings of Q3 preserve the same geometry for both states and have been omitted for simplicity.

The fluorescence properties exhibited by Q2 and Q3 can be related to their molecular structure. Lowering of the temperature restricts rotational vibrations (i.e., distortions from planarity) in S_1 and makes radiative $S_1 \rightarrow S_0$ vibronic coupling more effective. The same impediment to conformational flexibility on cooling inhibits intersystem crossing, which is one of the most effective radiationless pathways in oligothiophenes, and enhances the fluorescence activity. At the same time, internal conversion by vibrational relaxation is also intrinsically diminished, since the active vibrational modes are blocked. All these factors explain the fact that fluorescent emission appears at low temperatures. In line with this, the narrower HOMO–LUMO energy gap found for Q3 (1.67 eV compared with 2.16 eV for Q2) facilitates internal conversion and justifies the weaker fluorescence recorded for Q3. As for the intersystem crossing, this would lead to energy transfer to the triplet excited-state manifold and to population of the T_1 state by $T_n \rightarrow T_1$ internal conversion. The T_1 state plays a very important role in the quinoidal Q*n* series. Phosphorescence measurements were carried out for Q2 and Q3 in time-delay mode to detect the phosphorescent emission from T_1 and no signal was recorded up to 900 nm. As discussed above, calculations predict S_0–T_1 energy gaps smaller than 1.0 eV (see Table 1) that place this transition well into the NIR region out of our experimental spectral window.

Figure 7 compares the absorption and emission properties of quinoidal Q3 and its aromatic counterpart T3. This allows us to evidence the opposite pattern inherent in all the electronic properties of these two families of compounds. The absorption spectrum of T3, defined by the properties of the heteroaromatic S_0 state, is similar to the profile of the emission spectrum of Q3, since the S_1 state in this case has heteroaromatic character. This similarity is even clearer for the absorption spectrum of Q3 resulting from the quinoidal S_0 ground state, which very much resembles the emission spectrum of T3 (S_1 is of quinoidal character for T3, see Figure 6), and the vibronic structure of both spectra has a similar three-peak pattern.

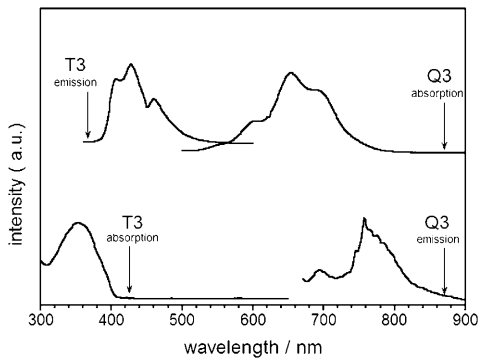

Figure 7. Comparison of the absorption and emission spectra of Q3 and T3.

Electrochemical data: Table 4 summarizes the redox potentials previously reported for Q2–Q6 by some of us,[4] together with the monoelectronic energies calculated for the HOMO and the LUMO. The data obtained for Q1, the first member of the series with only one thiophene ring, are included for the sake of comparison. In a first approach, Koopman's theorem enables us to relate the HOMO and LUMO energies with the electrochemical potentials of the first oxidation and reduction processes, respectively.[15]

Table 4. Electrochemical data, HOMO/LUMO energies, and HOMO–LUMO energy gap (E_{H-L}) for Q1–Q6.

Compound	$E^{red}_{1/2}$ [V][a]	$E^{ox}_{1/2}$ [V][a]	E_{HOMO} [eV][b]	E_{LUMO} [eV][b]	E_{H-L} [eV][b]
Q1	−0.09, −0.65	–	−6.97	−4.07	2.90
Q2	−0.21, −0.46	–	−5.88	−3.72	2.16
Q3	−0.28[c]	1.18	−5.22	−3.55	1.67
Q4	−0.21[c]	0.80, 1.45[d]	−4.78 (−4.86)	−3.45 (−3.40)	1.33 (1.46)
Q5	−0.16[c]	0.55, 1.05	−4.46 (−4.65)	−3.40 (−3.28)	1.06 (1.37)
Q6	−0.12[c]	0.38, 0.78	−4.21 (−4.48)	−3.38 (−3.19)	0.83 (1.29)

[a] Half-wave redox potentials from ref. [4] measured in benzonitrile solution (reference electrode: Ag/AgCl). [b] RB3LYP/6-31G** monoelectronic energies (open-shell UB3LYP(BS)/6-31G** values are given in parentheses for Q4–Q6). [c] Bielectronic process. [d] Irreversible.

All compounds except Q1 and Q2 display reversible amphoteric redox behavior due to the combination of electron-donor and electron-acceptor groups in the conjugated skeleton. Q2 exhibits two reversible one-electron reduction waves at −0.21 and −0.46 V that are much closer than those recorded for Q1 (−0.09 and −0.65 V). From Q3 onwards, the two waves combine in a bielectronic process that shifts to less negative potentials with increasing oligomer size. Q3 to Q6 show reversible first oxidation waves that evolve to lower anodic potentials as the chain length increases. For Q4–Q6, a second oxidation wave is also observed.

Calculations predict that both the HOMO and LUMO increase in energy with increasing oligomer length. This trend is found in both the CS and the OS solutions of S_0, that is, in a first approach, the biradical character of the ground state is not a key factor that determines the electrochemical response of quinoidal molecules. However, the OS solution predicts larger HOMO–LUMO energy gaps for Q4–Q6, as expected from the aromatization of their structures.

The increase in the LUMO energy explains the shift to higher cathodic potentials observed for the first reduction wave on passing from Q1 to Q2, but does not justify the shift to lower cathodic potentials recorded from Q3 to Q6. The reason for this apparent discrepancy is that Koopman's theorem is a one-electron approach and does not apply to the reduction processes of Q3–Q6, which involve two electrons. Qualitatively, one might expect that the addition of new thiophene units, thereby electron-enriching the central oligothienyl spine, to progressively mitigate the electron-ac-

ceptor character of the terminal dicyanomethylene groups and therefore reduce the electron affinity of the whole π-conjugated system. This is what the energy of the LUMO of Q*n* compounds suggests and what is actually measured for a family of aromatic oligothiophenes end-capped in the α-positions with nitrile groups (T*n*CN2), for which the first reduction potential shifts to more negative values as the oligomer lengthens (T2CN2: −1.88, T3CN2: −1.94, T4CN2: −2.01 V).[16] The opposite trend found for Q3–Q6 is due to Coulombic interactions and to the quinoid structure of these compounds. On the one hand, the two electrons introduced to form the dianion are mainly incorporated into the dicyanomethylene groups, and the decreasing Coulombic repulsion with increasing oligomer length thus facilitates the reduction process. On the other hand, reduction causes aromatization of the quinoid structure (see Figure S3 in the Supporting Information), an energetically favorable process whose effect increases with increasing number of thiophene rings and stabilizes the reduced species.[2,8] These two factors determine that dianions instead of singly charged anions are directly formed on reduction of Q3–Q6.

The oxidation potentials measured for Q3–Q6 decrease with increasing oligomer length, in agreement with the tendency found for the HOMO energy and Koopman's approach. In this case, the processes are monoelectronic and no charge repulsions must be taken into account. Despite the stronger electron-withdrawing character of the $C(CN)_2$ groups, the potentials recorded for Q3 (1.18), Q4 (0.80), and Q5 (0.55 V) are similar to those reported for aromatic T3CN2 (1.06), T4CN2 (0.78), and T5CN2 (0.66 V).[16] This effect must be ascribed to partial aromatization of the quinoid backbone on oxidation (see Figure S3 in the Supporting Information).[2] The quinoid structure of compounds Q2–Q6 therefore has a remarkable effect on the redox potentials, more pronounced than that expected by only introducing electron-acceptor groups stronger than the CN group,[17] since the anodic potentials are greatly shifted to more positive values without significant alteration of the cathodic potentials.

To further investigate the influence of the nature of the electronic ground state on the redox properties, we made use of Coulomb's law to analyze the electrostatic repulsion energy between two charges, which is directly proportional to the product of the charges and inversely proportional to the distance between them. Assuming that the extra electrons introduced on reduction will separate as much as possible in the molecule to avoid interelectronic repulsions, the first factor is a constant for Q*n* dianions and the second can be taken as the length of the long molecular axis. Under these assumptions, the reduction potentials of Q*n* compounds are inversely proportional to the molecular length ($V \propto r^{-1}$). Figure 8a shows the evolution of the cathodic response with chain length.

The reduction potentials of Q1–Q6 are correlated in Figure 8b with the adiabatic electron affinities (EA), estimated as the energy difference between the minimum-energy optimized structures calculated for the neutral molecule and for the dianionic species (Q1: 1.34, Q2: 1.94, Q3: 2.42, Q4: 2.78, Q5: 3.02, Q6: 3.19 eV). A linear correlation (regression coefficient $R^2 = 0.9874$) exists between the EA values and the reduction potentials. Nonetheless, a better fit is obtained by separating the Q*n* family into two groups: Q1–Q3 ($R^2 = 0.9978$) and Q4–Q6 ($R^2 = 0.9984$). Figure 8a and b then suggest a different behavior for the longest systems, for which the biradical character of the singlet ground state grows with increasing chain length.

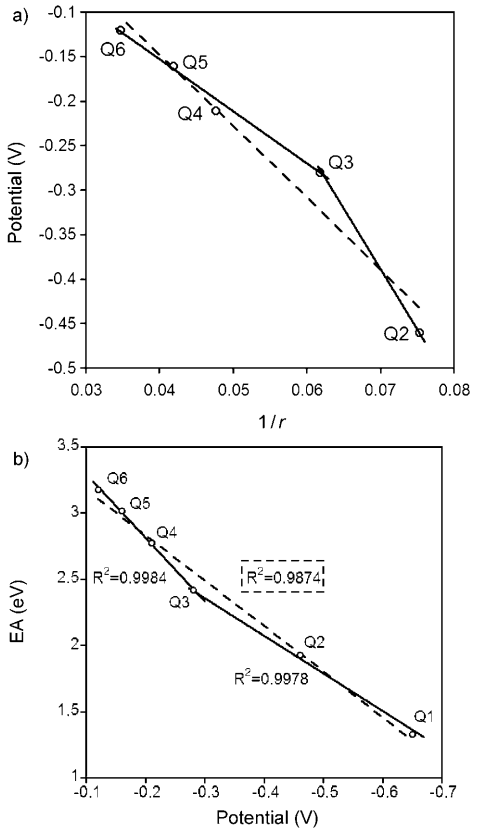

Figure 8. a) Evolution of the reduction potentials of Q*n* compounds with reciprocal molecular length $1/r$ [Å^{-1}]. b) Adiabatic electron affinities estimated as $E_{neutral} - E_{dianion}$ versus reduction potentials of Q*n*. Reduction processes are bielectronic for Q3–Q6 and the value of the second reduction potential was used for Q1 and Q2.

Infrared spectroscopy: Figure 9 shows FTIR spectra of Q2–Q6 recorded as KBr pellets, and Figure 10 displays the theoretical IR spectra calculated at the RB3LYP level for Q2 and Q3 and at the open-shell UB3LYP(BS) level for Q4, Q5, and Q6.

The IR spectra of the shortest oligomers, Q2 and Q3, are quite similar owing to the quinoidal structure of the ground state. Both show three bands with noticeable intensity. The band registered around 1110 cm^{-1} arises from a vibration located on the lateral bis(butoxymethyl)cyclopentane groups (e.g., see the calculated eigenvectors for Q3 in Figure 11). The most intense band appearing at 1511 (Q2) and 1471 cm^{-1} (Q3) is due to a collective asymmetrical C–C vi-

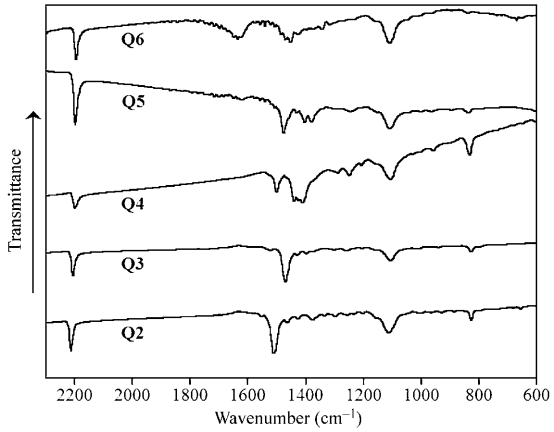

Figure 9. FTIR spectra of Q*n* recorded as KBr pellets.

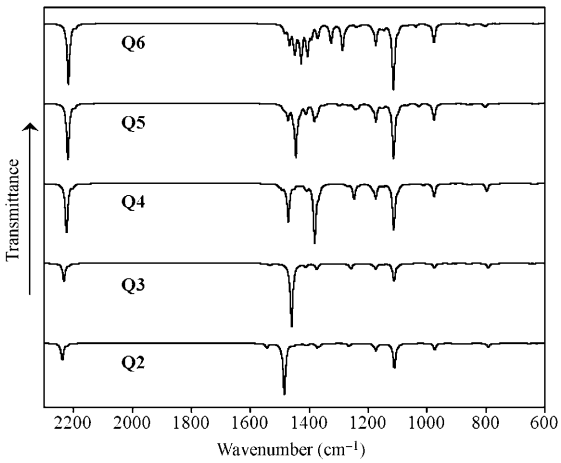

Figure 10. Theoretical IR spectra calculated at the B3LYP/6-31G** (Q2 and Q3) and UB3LYP(BS)/6-31G** (Q4, Q5, and Q6) levels.

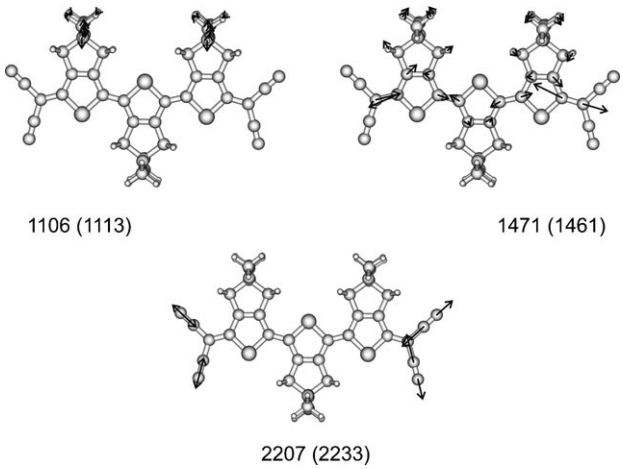

Figure 11. B3LYP/6-31G** IR-active vibrational eigenvectors calculated for Q3. Experimental and theoretical (in parentheses) wavenumbers are given in reciprocal centimeters.

bration that spreads along the entire conjugated skeleton with a large contribution from stretching of the terminal dicyanovinylene double bonds. Finally, the band registered around 2210 cm^{-1} corresponds to the stretching vibration of the C≡N bonds.

In the case of the longest oligomers, it is necessary to take into account the theoretical spectra calculated with the open-shell UB3LYP(BS) approach to account for the existence and relative intensities of the experimental bands (the CS solution predicts spectral profiles simpler than those registered experimentally; see Figure S4 in the Supporting Information). Nonetheless, minor discrepancies exist between experimental and theoretical spectra that are more pronounced for Q4. Since Q4 represents the frontier between the CS and OS solutions of S_0, this could explain the inaccuracy of the theoretical prediction. For instance, the group of three experimental bands around 1440–1410 cm^{-1} is predicted as one quite intense band (1391 cm^{-1}) by the OS solution (see Figures 9 and 10).

Theoretical eigenvectors indicate that the band registered around 1110 cm^{-1} is due, as for the shortest members of the family, to a vibration localized on the lateral bis(butoxymethyl)cyclopentane groups, and its position does not change with the quinoid or aromatic structure of the oligomer. In contrast, the bands around 1350–1500 cm^{-1} spread all over the conjugated backbone and their position and structure change with the oligomer. The ν(CN) band is recorded at 2199 cm^{-1} for Q4 and Q5 and at 2196 cm^{-1} for Q6. The position of this band is highly sensitive to the electron density borne by the CN bonds, and its shift to lower frequencies for the tetracyano-*p*-quinodimethane (TCNQ) molecule on complexation with electron donors has been related in the past to the degree of charge transfer in organic conductive salts.[18] The CN stretch is measured at 2225 cm^{-1} for neutral TCNQ, 2197 cm^{-1} for $TCNQ^-$, and 2164 cm^{-1} for $TCNQ^{2-}$.[19] By using these data as reference, it is possible to infer the amount of ground state polarization to the $C(CN)_2$ groups from the frequencies measured for the ν(CN) vibrations. Table 5 collects the values of the ν(CN) frequencies for compounds Q2–Q6 and compares the net charges deduced for the terminal $C(CN)_2$ groups from the experimental frequencies with the theoretically-calculated Mulliken charges.

Table 5 shows that although calculations slightly overestimate the ν(CN) frequencies, experimental and theoretical

Table 5. Experimental and theoretical (B3LYP/6-31G**) stretching vibrations of the CN group. EC: experimental net charge per $C(CN)_2$ group calculated from the dispersion of ν(CN). TC: theoretical Mulliken net charge per $C(CN)_2$ group. Optimized bond lengths for the CN triple bond.

Compound	$\nu(CN)_{exptl}$ [cm^{-1}]	$\nu(CN)_{theor}$ [cm^{-1}][a]	EC [e]	TC [e][a]	d(C≡N) [Å][a]
Q2	2213	2238	−0.214	−0.293	1.165
Q3	2207	2233	−0.321	−0.333	1.166
Q4	2199	2224	−0.464	−0.348	1.167
Q5	2199	2220	−0.464	−0.354	1.167
Q6	2196	2218	−0.517	−0.361	1.168

[a] RB3LYP values are given for Q2 and Q3 and UB3LYP(BS) values for Q4–Q6.

ν(CN) data follow the same trend with similar dispersion values (17 and 20 cm^{-1}, respectively). As expected, the ν(CN) vibration appears at lower frequencies as the oligomer gets longer due to the increasing ease of polarizing the π-electron cloud towards the electron-withdrawing dicyanomethylene groups. The net charge per dicyanomethylene group indeed increases with increasing chain length, which correlates with softening of the CN triple bonds and suggests greater ground-state polarization in the molecular system. These results indicate that by inserting thiophene rings it is possible to modulate the electron-density drift or polarization towards the electron-withdrawing groups from the central spine.

Let us now continue with the analysis of the relative intensity and position of the most intense IR bands on lengthening of the molecule. The band recorded at 1511 cm^{-1} in Q2 downshifts to lower frequencies and undergoes band splitting with increasing oligomer size. For instance, it appears as a less intense, two-peak structure at 1405 and 1380 cm^{-1} for Q5. In a similar way, the small band observed at 1552 cm^{-1} for Q2 seems to downshift (1477 cm^{-1} for Q5) and to increase in intensity with chain length. These changes are assigned to the appearance of two different structural domains in the long quinoidal systems provoked by stabilization of the biradical form (see BLA values in Table 2). For Q4, the band at 1501 cm^{-1} due to the aromatic domain is less intense that those corresponding to quinoidal-type vibrations (1410–1440 cm^{-1}), that is, the quinoidal structure represents a very important part of the molecule. On the contrary, the aromatic bands of Q5 (1477 cm^{-1}) and Q6 (1455 cm^{-1}) gain in intensity at the expense of the quinoidal bands, in support of the greater aromatization predicted by OS calculations for Q5 and Q6 (see Figure 1 and Table 2). On the other hand, the band registered around 1110 cm^{-1} increases in relative intensity with increasing oligomer length. This trend is well reproduced by theoretical calculations assuming CS solutions for Q2 and Q3 and OS solutions for Q4–Q6 (see Figure 10).

Infrared spectroscopy is therefore a sensitive technique to determine the electronic nature of the ground state of quinoid systems. The FTIR data support the quinoidal structures predicted theoretically for Q2 and Q3 and the more aromatic, open-shell biradical structures obtained for Q4–Q6. However, IR spectroscopy does not provide any evidence for thermally accessible triplet states that account for the magnetic activity of the longest members of the Q*n* family.[4]

Raman spectroscopy: To explain the magnetic signal recorded by EPR experiments, Raman spectroscopy and, in particular, resonance Raman spectroscopy can be especially useful due to their high sensitivity, which allows determination of species with sample concentrations as low as 10^{-8} M. In resonance Raman spectroscopy, the energy of the incoming laser is adjusted such that the scattered light fits with an electronic transition of the molecule.[20] Thereby, rather than exciting the molecule to a virtual energy state (Raman spectroscopy), in resonance Raman spectroscopy the molecule is excited to the energetic vicinity of one of its excited electronic states. As a consequence, the vibrational modes that reproduce the geometrical changes involved in the electronic transition exhibit greatly increased Raman scattering intensity. This aspect of resonance Raman spectroscopy is especially useful for tackling our problem, since the triplet state is populated only in small relative amounts.

In this section we first analyze the FT Raman spectra of Q*n* compounds, and then we combine electronic and Raman spectra to register Raman spectra in resonance by choosing the excitation wavelength. These experiments are very helpful for obtaining further information on the electronic structure of the ground and excited states of the Q*n* heteroquinoid systems.

Figure 12b displays the FT Raman spectra of Q*n* recorded at low temperatures (−150 °C) to avoid contribution from triplet biradicals by thermal population of the T_1 state.

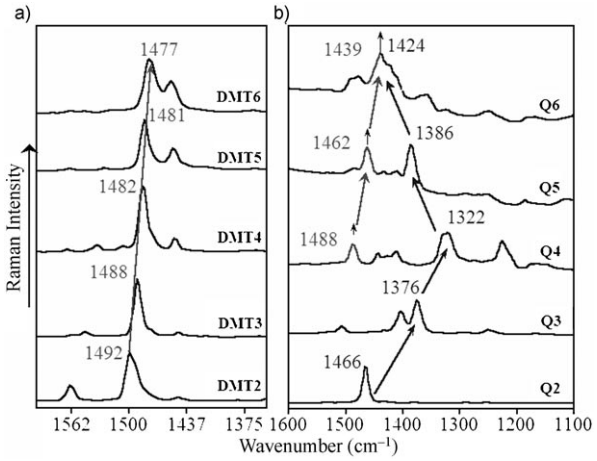

Figure 12. a) FT Raman spectra of a family of aromatic α,α′-dimethyloligothiophenes (DMT*n*). b) FT Raman spectra of Q*n* recorded at −150 °C. Arrows indicate band evolution with increasing length of the oligomer.

In the first stage, these spectra were used to find experimental Raman evidence for a contribution of the singlet biradical to the electronic structure of S_0, as suggested by theoretical calculations and by electronic and vibrational IR spectroscopy.

As shown in Figure 12, the evolution of the spectra of Q*n* compounds with increasing the length of the oligomer drastically differs from that recorded for a series of aromatic oligothiophenes end-capped in α-positions with methyl groups (DMT*n*).[21] For DMT*n* compounds, the most intense band, which arises from a collective vibration of the C−C/C=C skeleton and appears around 1500–1450 cm^{-1}, downshifts as the oligomer lengthens due to the more extended π-conjugation.[22] In our heteroquinoid systems, this behavior is observed from the dimer to the tetramer, for which new bands are observed. The tetramer behaves as an inflection point

between Q2/Q3 and Q5/Q6. The experimental spectra of Q2 and Q3 are in good agreement with the theoretical (CS) simulations (see Figure 13), with some discrepancies in intensity in the case of Q3. The FT Raman spectra therefore support the quinoid structure predicted theoretically for the shortest members of the Q*n* family.

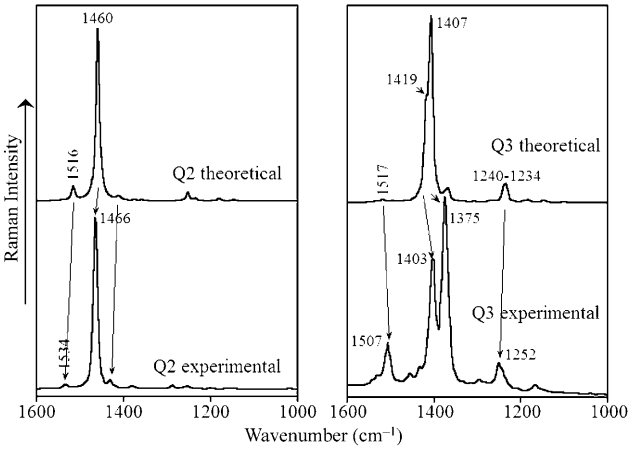

Figure 13. Experimental and theoretical (CS solution of S_0) Raman spectra of Q2 (left) and Q3 (right).

Theoretical B3LYP calculations however fail in simulating the experimental Raman spectra of the longest systems (see Figure S5 in the Supporting Information). Previous studies on Raman spectra of oligothiophenes in different oxidation states indicate that the shift of the most intense band towards higher frequencies demonstrates aromatization of the structure.[23] The appearance of active Raman bands in the aromatic frequency region for the longest Q*n* members (1488, 1462, and 1440–1420 cm^{-1} for Q4, Q5, and Q6, respectively) thus supports that aromatization of the S_0 state arises from the contribution of the singlet biradical form. These bands follow the same trend recorded for DMT*n* compounds, which indicates enlargement of the aromatic defect for long quinoidal systems, in good agreement with the BLA values reported in Table 2. This supports the reliability of the theoretical model used to calculate the electronic and molecular structures of Q*n*, although B3LYP calculations do not account properly for the Raman intensities of open-shell systems.

We now discuss thermal population of the T_1 triplet state in Q6, as an example of a long quinoidal oligothiophene. Figure 14 displays the electronic absorption spectra of Q6 together with the most intense singlet–singlet (from S_0) and triplet–triplet (from T_1) electronic transitions taken from TD-DFT calculations in Table 3. Figure 14 indicates that the laser wavelength can be carefully chosen to selectively register the resonance Raman spectrum of Q6 molecules in the singlet biradical S_0 state and of those populating the triplet T_1 state. In particular, the use of a visible 514 nm laser, that is closer to the $T_1 \rightarrow T_7$ electronic transition at 527 nm of the triplet state, leads to the spectrum shown in Figure 15 a. The

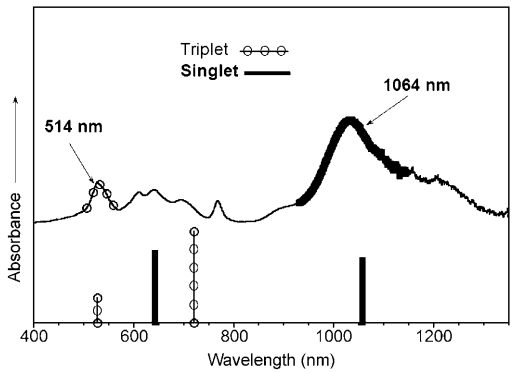

Figure 14. UV/Vis/NIR absorption spectrum of Q6 and TDDFT electronic transitions calculated for Q6 as an open-shell singlet (black bar) and as a triplet (solid line with circles). For simplicity, excitations with oscillator strengths lower than 0.4 have been omitted.

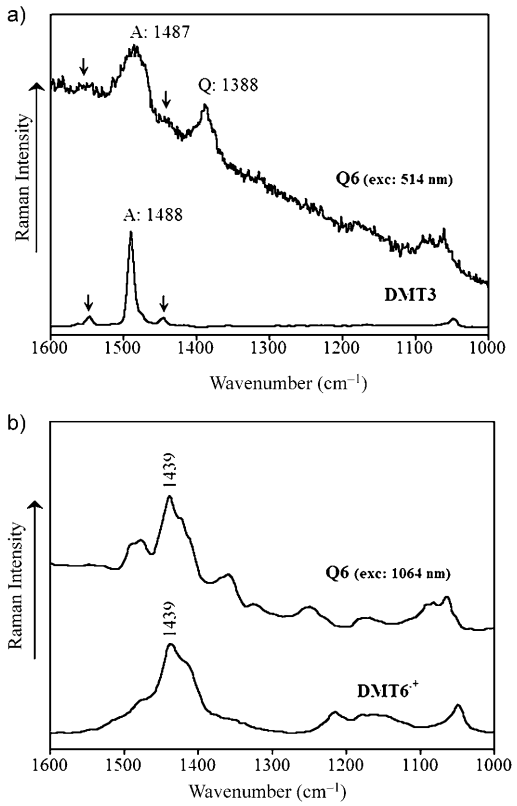

Figure 15. a) Resonance Raman spectrum (λ_{exc} = 514 nm) recorded for Q6 and FT Raman spectrum (λ_{exc} = 1064 nm) of DMT3. b) FT Raman spectra (λ_{exc} = 1064 nm) recorded for Q6 and the radical cation of DMT6.

spectral profile shows remarkable differences to that recorded with a 1064 nm NIR laser, which resonates with the $S_0 \rightarrow S_1$ electronic transition (Figure 15 b). Great similarity is found between the 514 nm spectrum and that recorded for the aromatic α,α′-dimethylterthiophene (DMT3).[20] The most intense band appears around 1488 cm^{-1} in both spectra, although in the Q6 spectrum is still possible to differentiate bands belonging to a less aromatic structure (1388 cm^{-1}) or to the contribution of the singlet biradical

species, which exhibits a low-intensity absorption at 543 nm ($f=0.16$). The similarity of the spectra of Q6 and DMT3 provides an empirical estimate of the aromatic defect created by population of the triplet T_1 state of Q6, and indicates that three of the six thiophene rings of the triplet biradical have an aromatic structure. This estimation is in accord with theoretical UB3LYP/6-31G** calculations (Table 2 and Figure 16), which predict that the four central thiophene rings of the triplet state have a pseudo-aromatic structure.

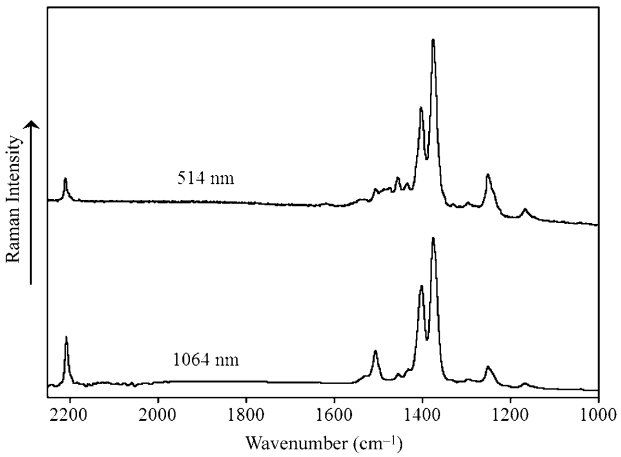

Figure 16. Raman spectrum of Q3 recorded with different laser excitations (514 and 1064 nm).

The 1064 nm spectrum of Q6 shown in Figure 15b is correlated with the corresponding spectrum of the radical cation of α,α′-dimethylsexithiophene (DMT6),[24] which, as theoretical calculations predict, displays a quinoidal-type geometry for the central two rings, a partially aromatic structure for the outermost two rings, and an intermediate situation in the remaining thiophene residues (Scheme 3). This predicted geometry explains the similarity found between the two spectra, as the singlet biradical of Q6 presents the same geometry but alternating positions of the aromatic/quinoid rings.

To further demonstrate population of the triplet state for the longest oligomers, the Raman spectrum of Q3, for which no thermal population of T_1 is expected, was registered with excitation wavelengths of 514 and 1064 nm. Figure 16 shows that the spectral profile of Q3 remains mostly unaffected on changing the laser excitation, in agreement with theoretical calculations, which predict that the T_1 state lies 9.88 kcal mol^{-1} above the S_0 state.

Raman spectra have thus demonstrated the existence of a populated triplet state for the longest oligomers. The next step is to analyze the thermal equilibrium between the S_0 and T_1 states. The population of the T_1 state can be determined by making use of a Boltzmann distribution and the calculated energy differences $\Delta E(T_1-S_0)$ given in Table 1. At 25 °C, the populations estimated for T_1 are 23.5% for Q6, 3.6% for Q5, and 0.057% for Q4, and no significant

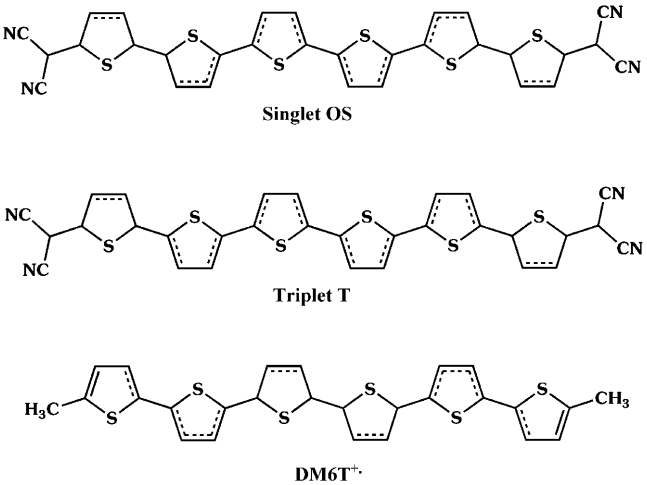

Scheme 3. Theoretical structures calculated for the singlet S_0 (OS solution) and triplet T_1 states of Q6 (lateral groups have been omitted for simplicity), and for the radical cation of DMT6. Bond lengths shorter than 1.385 Å and longer than 1.400 Å are considered to be double and single bonds, respectively. Dashed lines indicate intermediate situations.

population is obtained for Q2 and Q3. These results suggest that different behavior of the Raman spectra with temperature should be observed for Q4 and Q6. At room temperature, the T_1 state is highly populated for Q6 while it remains mostly unpopulated for Q4. A rise in temperature from 25 to 120 °C provokes an increase of the estimated population, which reaches 0.45% in the case of Q4 (this percentage could be detected by resonance Raman spectroscopy) and 34.8% for Q6. To support these theoretical data, Figure 17 displays the evolution of the Raman profile of Q4 and Q6 with temperature.

At high temperatures, the spectrum of Q4 shows relative enhancement of the more aromatic bands (around 1490 cm^{-1}) due to the triplet state compared to the quinoidal bands (around 1300 cm^{-1}) arising from molecules in the singlet state. On the contrary, the spectral profile of Q6 remains almost unaltered with temperature, with slight changes in relative intensities. This is due to population of the T_1 state of Q6 in the whole range of temperatures (the estimated population at −170 °C is 0.41%, already detectable by resonance Raman spectroscopy), and supports the existence of very low energy, thermally accessible, excited triplet states, which are responsible for the magnetic activity of long quinoidal thienyl molecules.

Conclusions

The geometrical, vibrational, and optical properties of a family of quinoidal oligothiophenes with two to six thiophene rings have been analyzed both experimentally and theoretically. Theoretical calculations indicate that the ground electronic state is always a singlet state. For the shortest oligomers, Q2 and Q3, the electronic structure is well described by the closed-shell solution of the wave func-

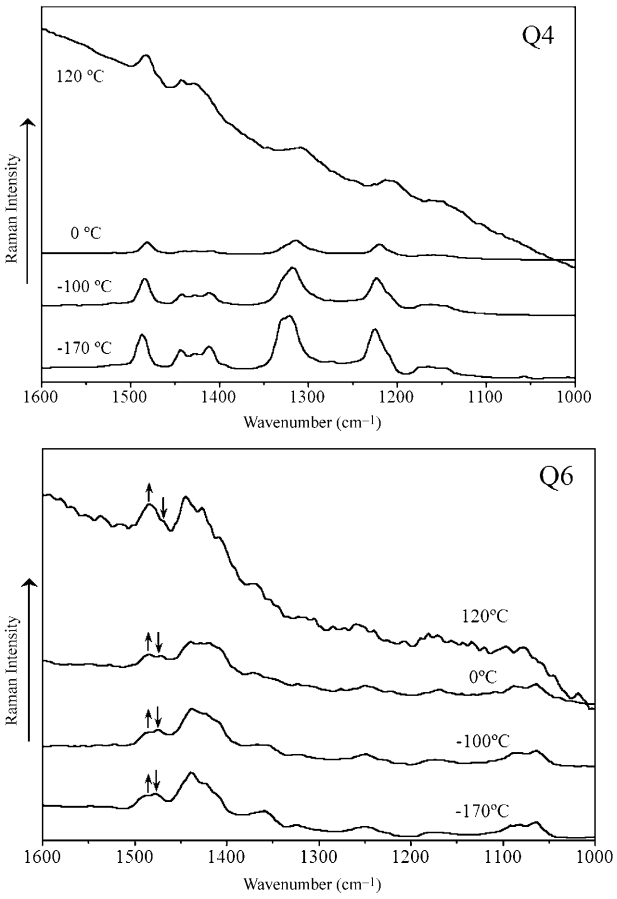

Figure 17. Evolution of the Raman spectra of Q4 and Q6 with temperature, from −170 °C to 120 °C.

tion, while the higher stability of the open-shell solution for the longest oligomers, Q4 to Q6, indicates a biradical character that increases with increasing oligomer length. Furthermore, the existence of a low-lying triplet state very close in energy to the singlet ground state is predicted. Electronic and vibrational (IR and Raman) spectra completely support the quinoidal structures computed for Q2 and Q3 and the aromatic biradical structures predicted for Q5 and Q6, and Q4 represents the inflexion point between closed-shell quinoid structures and aromatic biradicals. On the other hand, temperature-dependent experiments demonstrate population of a thermally accessible triplet state for Q4–Q6. Electrochemical experiments also suggest different behavior with increasing chain length, which again supports different natures of the ground state depending on the number of thiophene rings.

Experimental and Computational Section

UV/Vis/NIR absorption spectra were recorded at room temperature by means of an Agilent 8453 instrument equipped with a diode array for fast recording of all electromagnetic absorptions in the 190–1100 nm spectral region. A variable-temperature Specac P/N 21525 cell with quartz windows was used to record the UV/Vis/NIR spectra at different temperatures. This cell consists of a surrounding vacuum jacket (0.5 Torr) and combines a refrigerant Dewar and a heating block as the sample holder, which allow temperatures between −170 °C and +150 °C to be achieved. Samples were inserted into the Dewar/cell holder assembly as a solution in a 1×1 quartz cell and spectra were recorded after waiting for thermal equilibrium of the sample.

Emission spectra were measured on a Spectrofluorimeter from Edinburgh Analytical Instruments (FLS920P) equipped with a CW 450 W Xenon arc lamp, which generates spectra in the 200–900 nm range. A variable-temperature liquid-nitrogen cryostat from Oxford Instruments (Optistat DN) was connected with the spectrometer control software to perform low-temperature experiments. Gate phosphorescence spectra in frozen 2-methyltetrahydrofuran at −170 °C were recorded at delay times of >0.5 μs and a gate width of 2 ms. A pulsed xenon flash lamp was used for excitation.

FTIR absorption spectra were recorded on a Bruker Equinox 55 spectrometer. Compounds were ground to a powder and pressed in KBr pellets. FTIR spectra, with a standard spectral resolution of 2 cm^{-1}, were collected as the average of 50 scans. Interference from atmospheric water vapor was minimized by purging the instrument with dry nitrogen before starting data collection.

FT Raman scattering spectra were collected on a Bruker FRA106/S apparatus with a Nd:YAG laser source (λ_{exc}=1064 nm) in a backscattering configuration. The operating power for the exciting laser radiation was kept to 100 mW in all the experiments. Samples were analyzed as pure solids, and 1000 scans with 2 cm^{-1} of spectral resolution were averaged. Resonance Raman spectra (λ_{exc}=514 nm) were recorded with a Renishaw InVia Reflex Raman microscope.

All theoretical calculations were carried out with the Gaussian 03 program package.[25] Calculations were performed by a DFT approach using Becke's three-parameter B3LYP exchange-correlation functional[26] and the 6-31G** basis set.[27] The chemical structure of Q*n* compounds was simplified by substituting the pendant butoxymethyl groups by methoxymethyl groups. This structural change is not expected to affect the electronic properties and reduces considerably the number of atoms (from 286 to 178 for Q6) and the size of the basis set (from 2754 to 1854 atomic orbitals for Q6). The geometries of Q*n* were fully optimized with C_{2v} (odd-numbered oligomers) and C_{2h} (even-numbered oligomers) symmetry restrictions. Release of the symmetry constraints did not change the geometries, and the molecules remained mainly planar, as was tested for the trimer Q3.

Q*n* compounds were first calculated as closed-shell (CS) singlets at the spin-restricted RB3LYP/6-31G** level. The stability of the RB3LYP/6-31G** wave function was checked and it was found to become unstable (RHF to UHF instability)[28] for Q4, Q5, and Q6. Q*n* compounds were then reoptimized as open-shell (OS) singlets by using an spin-unrestricted broken-symmetry (BS) UB3LYP(BS)/6-31G** function. This approach uses the Guess=mix keyword to build up, as the initial guess wave function, a 1:1 mixture of the singlet and triplet states, with a spin-squared expectation value of $<S^2>=1$,[29] and has been shown to provide reliable geometries and energies for singlet-state biradicals.[30] Q*n* compounds were finally optimized as triplets at the UB3LYP/6-31G** level. Q*n* oligomers were also calculated as OS anions (UB3LYP/6-31G**) and CS dianions and dications (B3LYP/6-31G**). The shortest oligomers Q2 and Q3 were also optimized in the lowest-energy excited singlet state S_1 by using the Guess=alter keyword, to have an occupation number of one electron in both the HOMO and the LUMO, and imposing symmetry restrictions. Solvent effects were considered within the self-consistent reaction field (SCRF) theory by recalculating the B3LYP optimized geometries of S_0 and T_1 in $CHCl_3$ and using the polarized continuum model (PCM) to simulate the interaction with the solvent.[31]

Vertical electronic excitations energies were computed by using the time-dependent DFT (TDDFT) approach,[32] which provides excitation energies in good agreement with experiment for the low-lying valence excited states of most closed-shell compounds,[33] and has been successfully applied for singlet biradical compounds.[34] $S_0 \rightarrow S_n$ excitation energies were calculated at both the RB3LYP/6-31G** and the UB3LYP(BS)/6-31G**

levels by using the geometries optimized for S_0 at the respective levels of theory. $T_1 \rightarrow T_n$ excitation energies were obtained at the UB3LYP/6-31G** level by using the optimized geometry of T_1.

The calculated harmonic vibrational frequencies were scaled down uniformly by a factor of 0.96, as recommended by Scott and Radom.[35] All theoretical vibrational data quoted in the text are thus scaled values. The theoretical IR and Raman spectra were obtained by convoluting the scaled frequencies with Gaussian functions (10 cm^{-1} width at half-maximum). The height of the Gaussians was determined from the IR intensities and Raman scattering activities calculated for the IR- and Raman-active normal modes, respectively.

Acknowledgements

Financial support by the MICINN of Spain (projects CTQ2006-14987-C02-01, CTQ2006-14987-C02-02, and Consolider-Ingenio CSD2007-00010 in Molecular Nanoscience), the Junta de Andalucia (project 2006/FQM1678), the Generalitat Valenciana (grant GVAINF/2007/051), and European FEDER funds (project CTQ2006-14987-C02) is gratefully acknowledged. R.P.O. thanks the MICNN of Spain for a personal postdoctoral fellowship.

[1] a) T. M. Pappenfus, R. J. Chesterfield, C. D. Frisbie, K. R. Mann, J. Casado, J. D. Raff, L. L. Miller, *J. Am. Chem. Soc.* **2002**, *124*, 4184; b) T. M. Pappenfus, J. D. Raff, E. J. Hukkanen, J. R. Burney, J. Casado, S. M. Drew, L. L. Miller, K. R. Mann, *J. Org. Chem.* **2002**, *67*, 6015; c) R. J. Chesterfield, C. R. Newman, T. M. Pappenfus, P. C. Ewbank, M. H. Haukaas, K. R. Mann, L. L. Miller, C. D. Frisbie, *Adv. Mater.* **2003**, *15*, 1278.

[2] a) J. Casado, L. L. Miller, K. R. Mann, T. M. Pappenfus, H. Higuchi, E. Ortí, B. Milián, R. Pou-Amérigo, V. Hernández, J. T. López Navarrete, *J. Am. Chem. Soc.* **2002**, *124*, 12380; b) J. Casado, T. M. Pappenfus, K. R. Mann, E. Ortí, P. M. Viruela, B. Milián, V. Hernández, J. T. López Navarrete, *ChemPhysChem* **2004**, *5*, 529.

[3] Z. Bao, J. A. Rogers, H. E. Katz, *J. Mater. Chem.* **1999**, *9*, 1895.

[4] T. Takahashi, K.-I. Matsuoka, K. Takimiya, T. Otsubo, Y. Aso, *J. Am. Chem. Soc.* **2005**, *127*, 8928.

[5] T. Izumi, S. Kobashi, K. Takimiya, Y. Aso, T. Otsubo, *J. Am. Chem. Soc.* **2003**, *125*, 5286.

[6] a) K. Yui, Y. Aso, T. Otsubo, F. Ogura, *Bull. Chem. Soc. Jpn.* **1989**, *62*, 1539; b) K. Yui, H. Ishida, Y. Aso, T. Otsubo, F. Ogura, *Bull. Chem. Soc. Jpn.* **1989**, *62*, 1547; c) M. Fujii, Y. Aso, T. Otsubo, F. Ogura, *Synth. Met.* **1993**, *56*, 1910.

[7] a) H. Higuchi, T. Nakayama, H. Koyama, J. Ojima, T. Wada, H. Sasabe, *Bull. Chem. Soc. Jpn.* **1995**, *68*, 2363; b) H. Higuchi, S. Yoshida, Y. Uraki, J. Ojima, *Bull. Chem. Soc. Jpn.* **1998**, *71*, 2229.

[8] a) R. Ponce Ortiz, J. Casado, V. Hernández, J. T. López Navarrete, E. Ortí, P. M. Viruela, B. Milián, S. Hotta, G. Zotti, S. Zecchin, B. Vercelli, *Adv. Funct. Mater.* **2006**, *16*, 531; b) G. Zotti, S. Zecchin, B. Vercelli, A. Berlin, J. Casado, V. Hernández, R. P. Ortiz, J. T. López Navarrete, E. Ortí, P. M. Viruela, B. Milián, *Chem. Mater.* **2006**, *18*, 1539.

[9] R. Ponce Ortiz, J. Casado, V. Hernández, J. T. López Navarrete, P. M. Viruela, E. Ortí, K. Takimiya, T. Otsubo, *Angew. Chem.* **2007**, *119*, 9215; *Angew. Chem. Int. Ed.* **2007**, *46*, 9057.

[10] W. J. M. Naber, S. Faez, W. G. Van der Wiel, *J. Phys. D* **2007**, *40*, R205.

[11] a) T. Kubo, A. Shimizu, M. Sakamoto, M. Uruichi, K. Yakushi, M. Nakano, D. Shiomi, K. Sato, T. Takui, Y. Morita, K. Nakasuji, *Angew. Chem.* **2005**, *117*, 6722; *Angew. Chem. Int. Ed.* **2005**, *44*, 6564; b) T. Kubo, M. Sakamoto, K. Nakasuji, *Polyhedron* **2005**, *24*, 2522; c) T. Kubo, A. Shimizu, M. Uruichi, K. Yakushi, M. Nakano, D. Shiomi, K. Sato, T. Takui, Y. Morita, K. Nakasuji, *Org. Lett.* **2007**, *9*, 81.

[12] a) J. Casado, R. Ponce Ortiz, M. C. Ruiz Delgado, V. Hernández, J. T. López Navarrete, J.-M. Raimundo, P. Blanchard, M. Allain, J. Roncali, *J. Phys. Chem. B* **2005**, *109*, 16616; b) A. Berlin, S. Grimoldi, G. Zotti, R. Malavé Osuna, M. C. Ruiz Delgado, R. Ponce Ortiz, J. Casado, V. Hernández, J. T. López Navarrete, *J. Phys. Chem. B* **2005**, *109*, 22308.

[13] a) S. Hotta, K. Waragai, *J. Phys. Chem.* **1993**, *97*, 7427; b) W. Gebauer, M. Sokolowski, E. Umbach, *Chem. Phys.* **1998**, *227*, 33; c) J. Gierschner, H.-G. Mack, H.-J. Egelheaf, S. Schweizer, B. Doser, D. Oelkrug, *Synth. Met.* **2003**, *138*, 311.

[14] a) J. Casado, T. M. Pappenfus, L. L. Miller, K. R. Mann, E. Ortí, P. M. Viruela, R. Pou-Amérigo, V. Hernández, J. T. López Navarrete, *J. Am. Chem. Soc.* **2003**, *125*, 2524; b) E. Ortí, P. M. Viruela, R. Viruela, F. Effenberger, V. Hernández, J. T. López Navarrete, *J. Phys. Chem. A* **2005**, *109*, 8724.

[15] a) R. Ponce Ortiz, M. C. Ruiz Delgado, J. Casado, V. Hernández, O.-K. Kim, H. Y. Woo, J. T. López Navarrete, *J. Am. Chem. Soc.* **2004**, *126*, 13363; b) J. Casado, V. Hernández, M. C. Ruiz Delgado, R. Ponce Ortiz, J. T. López Navarrete, A. Facchetti, T. J. Marks, *J. Am. Chem. Soc.* **2005**, *127*, 13364; c) J. Casado, M. Z. Zgierski, P. C. Ewbank, M. W. Burand, D. E. Janzen, K. R. Mann, T. M. Pappenfus, A. Berlin, E. Pérez-Inestrosa, R. Ponce Ortiz, J. T. López Navarrete, *J. Am. Chem. Soc.* **2006**, *128*, 10134.

[16] J. Casado, R. Ponce Ortiz, M. C. Ruiz Delgado, R. Azumi, R. T. Oakley, V. Hernández, J. T. López Navarrete, *J. Phys. Chem. B* **2005**, *109*, 10115.

[17] J. Casado, M. C. Ruiz Delgado, M. C. Rey Merchán, V. Hernández, J. T. López Navarrete, T. M. Pappenfus, N. Williams, W. J. Stegner, J. C. Jonson, B. A. Edlund, D. E. Janzen, K. R. Mann, J. Orduna, B. Villacampa, *Chem. Eur. J.* **2006**, *12*, 5458.

[18] J. S. Chappell, A. N. Bloch, W. A. Bryden, M. Maxfield, T. O. Poehler, D. O. Cowan, *J. Am. Chem. Soc.* **1981**, *103*, 2442.

[19] a) T. Takenaka, *Spectrochim. Acta Part A* **1971**, *27*, 1735; b) A. Girlando, C. Pecile, *Spectrochim. Acta Part A* **1973**, *29*, 1859; c) E. Faulches, A. Leblanc, P. Molini, M. Decoster, F. Conan, J. E. Guerchais, J. Sala-Pala, *Spectrochim. Acta Part A* **1995**, *51*, 805; d) M. S. Khathake, J. P. Devlin, *J. Chem. Phys.* **1979**, *70*, 1851.

[20] a) E. Smith, G. Dent, *Modern Raman Spectroscopy. A Practical Approach*, Wiley, New York, **2005**; b) *Handbook of Raman Spectroscopy: From the Research Laboratory to the Process Line* (Eds.: I. R. Lewis, H. G. M. Edwards), Marcel Dekker, New York, **2001**.

[21] a) J. Casado, V. Hernández, F. J. Ramírez, J. T. López Navarrete, *Synth. Met.* **1997**, *89*, 159; b) V. Hernández, J. Casado, L. Favaretto, G. Distefano, J. T. López Navarrete, *Synth. Met.* **1999**, *101*, 548; c) V. Hernández, J. Casado, F. J. Ramírez, L. J. Alemany, S. Hotta, J. T. López Navarrete, *J. Phys. Chem.* **1996**, *100*, 289.

[22] a) A. Sakamoto, Y. Furukawa, M. Tasumi, *J. Phys. Chem.* **1994**, *98*, 4635; b) N. Yokonuma, Y. Furukawa, M. Tasumi, M. Kuroda, J. Nakayama, *Chem. Phys. Lett.* **1996**, *255*, 431; c) C. Moreno Castro, M. C. Ruiz Delgado, V. Hernández, Y. Shirota, J. Casado, J. T. López Navarrete, *J. Phys. Chem. B* **2002**, *106*, 7163; d) J. Casado, R. G. Hicks, V. Hernández, D. J. T. Myles, M. C. Ruiz Delgado, J. T. López Navarrete, *J. Chem. Phys.* **2003**, *118*, 1912; e) A. Milani, L. Brambilla, M. Del Zoppo, G. Zerbi, *J. Phys. Chem. B* **2007**, *111*, 1271.

[23] a) J. Casado, L. L. Miller, K. R. Mann, T. M. Pappenfus, V. Hernández, J. T. López Navarrete, *J. Phys. Chem. B* **2002**, *106*, 3597; b) J. Casado, M. C. Ruiz Delgado, Y. Shirota, V. Hernández, J. T. López Navarrete, *J. Phys. Chem. B* **2003**, *107*, 2637.

[24] J. Casado, V. Hernández, S. Hotta, J. T. López Navarrete, *Adv. Mater.* **1998**, *10*, 1458.

[25] Gaussian 03, Revision C.02, M. J. Frisch, G. W. Trucks, H. B. Schlegel, G. E. Scuseria, M. A. Robb, J. R. Cheeseman, J. A. Montgomery, Jr., T. Vreven, K. N. Kudin, J. C. Burant, J. M. Millam, S. S. Iyengar, J. Tomasi, V. Barone, B. Mennucci, M. Cossi, G. Scalmani, N. Rega, G. A. Petersson, H. Nakatsuji, M. Hada, M. Ehara, K. Toyota, R. Fukuda, J. Hasegawa, M. Ishida, T. Nakajima, Y. Honda, O. Kitao, H. Nakai, M. Klene, X. Li, J. E. Knox, H. P. Hratchian, J. B. Cross, V. Bakken, C. Adamo, J. Jaramillo, R. Gomperts, R. E. Stratmann, O. Yazyev, A. J. Austin, R. Cammi, C. Pomelli, J. W.

Ochterski, P. Y. Ayala, K. Morokuma, G. A. Voth, P. Salvador, J. J. Dannenberg, V. G. Zakrzewski, S. Dapprich, A. D. Daniels, M. C. Strain, O. Farkas, D. K. Malick, A. D. Rabuck, K. Raghavachari, J. B. Foresman, J. V. Ortiz, Q. Cui, A. G. Baboul, S. Clifford, J. Cioslowski, B. B. Stefanov, G. Liu, A. Liashenko, P. Piskorz, I. Komaromi, R. L. Martin, D. J. Fox, T. Keith, M. A. Al-Laham, C. Y. Peng, A. Nanayakkara, M. Challacombe, P. M. W. Gill, B. Johnson, W. Chen, M. W. Wong, C. Gonzalez, J. A. Pople, Gaussian, Inc., Wallingford CT, **2004**.

[26] A. D. Becke, *J. Chem. Phys.* **1993**, *98*, 1372.

[27] M. M. Francl, W. J. Pietro, W. J. Hehre, J. S. Binkley, M. S. Gordon, D. J. Defrees, J. A. Pople, *J. Chem. Phys.* **1982**, *77*, 3654.

[28] S. D. Kahn, W. J. Hehre, J. A. Pople, *J. Am. Chem. Soc.* **1987**, *109*, 1871.

[29] Open-shell singlets calculated using unrestricted broken-symmetry UDFT methods mix closed-shell and open-shell configurations and are not pure spin states. This is reflected by $\langle S^2 \rangle$ values that are different from 0 (pure singlet) and 2 (pure triplet).

[30] a) E. R. Davidson, *Int. J. Quantum Chem.* **1998**, *69*, 241; b) P. M. Lathi, A. S. Ichimura, J. A. Sanborn, *J. Phys. Chem. A* **2001**, *105*, 251; c) E. R. Davidson, A. E. Clark, *Int. J. Quantum Chem.* **2005**, *103*, 1.

[31] a) J. Tomasi, M. Persico, *Chem. Rev.* **1994**, *94*, 2027; b) C. S. Cramer, D. G. Truhlar in *Solvent Effects and Chemical Reactivity* (Eds.: O. Tapia, J. Bertrán), Kluwer, Dordrecht, **1996**, p. 1.

[32] a) E. Runge, E. K. U. Gross, *Phys. Rev. Lett.* **1984**, *52*, 997; b) E. K. U. Gross, W. Kohn, *Adv. Quantum Chem.* **1990**, *21*, 255; c) E. K. U. Gross, C. A. Ullrich, U. J. Gossmann in *Density Functional Theory* (Eds.: E. K. U. Gross, R. M. Driezler), Plenum Press, New York, **1995**, p. 149; d) M. E. Casida in *Recent Advances in Density Functional Methods, Part I* (Ed.: Chong, D. P.), World Scientific, Singapore, **1995**, p. 155.

[33] a) H. H. Heinze, A. Görling, N. Rösch, *J. Chem. Phys.* **2000**, *113*, 2088; b) M. Dierksen, S. Grimme, *J. Phys. Chem. A* **2004**, *108*, 10225; c) T. M. Halasinski, J. L. Weisman, R. Ruiterkamp, T. J. Lee, F. Salama, M. Head-Gordon, *J. Phys. Chem. A* **2003**, *107*, 3660.

[34] Y. Gao, C.-G. Liu, Y.-S. Jiang, *J. Phys. Chem. A* **2002**, *106*, 5380.

[35] A. P. Scott, L. Radom, *J. Phys. Chem.* **1996**, *100*, 16502.

Received: July 22, 2009
Published online: November 24, 2009

